Available online at www.sciencedirect.com
ScienceDirect
International Journal of Heat and Mass Transfer 50 (2007) 1010–1017
International Journal of HEAT and MASS TRANSFER
www.elsevier.com/locate/ijhmt

Buoyant instability in a laterally heated vertical cylinder

L.E. Gemeny [a,1], L. Martin Witkowski [b], J.S. Walker [a,*]

[a] Department of Mechanical and Industrial Engineering, University of Illinois, 1206 West Green St., Urbana, IL 61801, USA
[b] LIMSI-CNRS, BP 133, 91403 Orsay Cedex, France

Received 24 March 2006; received in revised form 27 July 2006
Available online 10 October 2006

Abstract

This paper presents a linear stability analysis for the buoyant convection in a vertical cylinder with isothermal top and bottom walls at the same temperature and with an axisymmetric heat transfer into the liquid from the vertical cylindrical wall. Results are presented for Prandtl numbers between 0.0 and 0.1 and for two different thermal boundary conditions at the vertical wall: a prescribed parabolic temperature variation or a prescribed parabolic radial heat flux variation. The results are radically different for the two thermal boundary conditions.

Keywords: Buoyant convection; Linear instability; Low Prandtl number

1. Introduction

For zonal-melting crystal growth, a polycrystalline feed rod is placed inside a vertical, cylindrical ampoule. The ampoule is moved slowly downward through an axisymmetric heater which creates a short length of molten semiconductor (melt) inside the ampoule. A single crystal grows inside the ampoule from the bottom of the melt below the heater. The feed-rod-melt interface and the crystal-melt interface are both isothermal at the same temperature, namely the solidification temperature, T_s. The radial temperature gradient associated with the heat input from the heater produces a steady, axisymmetric buoyant convection in the melt. If a hydrodynamic instability in the buoyant convection leads to a steady or periodic three-dimensional melt motion, the associated non-axisymmetric mass transport to the crystal greatly degrades the quality of the crystal. The buoyant instability cannot be eliminated by reducing the temperature difference in the melt because a minimum temperature gradient at the crystal-melt interface is required to maintain single crystal growth. Accurate models are needed to predict the buoyant instability, particularly for attempts to increase the diameter of the crystal or to increase the rate of crystal growth, where this rate determines the minimum temperature gradient required at the crystal-melt interface. The research on convective instabilities in crystal-growth processes has been reviewed by Imaishi and Kakimoto [1] and by Lappa [2].

This paper presents a linear stability analysis for the steady, axisymmetric buoyant convection in a vertical cylinder (a) with isothermal top and bottom walls at the same temperature, namely T_s, and (b) with an axisymmetric heat flux into the melt at the vertical cylindrical wall. We only consider small values of the Prandtl number Pr, namely $0.0 \leqslant Pr \leqslant 0.1$, because this range includes all the important semiconductors. We only consider a cylinder whose axial height equals its diameter because the aspect ratio of the melt zone in zonal-melting crystal growth is always close to this ratio. We use cylindrical coordinates r, θ, z with the z axis along the vertical centerline of the cylinder and with the origin at the center of the melt. We normalize r and z with the inside radius of the cylinder R, so that the liquid domain is $0 \leqslant r \leqslant 1$, $-1 \leqslant z \leqslant 1$. The dimensionless

* Corresponding author. Tel.: +1 217 333 7979; fax: +1 217 244 6534.
E-mail address: jswalker@uiuc.edu (J.S. Walker).
1 Present address: 3M Engineering Design Services, Bldg. 42-03E-03, 900 Bush Ave., St. Paul, MN 55106, USA.

0017-9310/$ - see front matter © 2006 Elsevier Ltd. All rights reserved.
doi:10.1016/j.ijheatmasstransfer.2006.07.026

Nomenclature

g	acceleration of gravity	t	time
Gr	Grashof number	$\mathbf{v}$	velocity
k	thermal conductivity	β	volumetric expansion coefficient
m	azimuthal wave number	ε	small parameter for perturbation
p	pressure	θ	azimuthal coordinate
Pr	Prandtl number	κ	thermal diffusivity
$q_{\max}$	maximum heat flux	λ	complex eigenvalue
r	radial coordinate	ν	kinematic viscosity
R	inside radius of cylinder	ρ	density
Ra	Rayleigh number	ψ_0	stream function for base flow

temperature T is the deviation of the dimensional temperature from T_s, normalized by some characteristic temperature difference, $(\Delta T)_c$, so that $T = 0$, at $z = \pm 1$. We consider two different thermal boundary conditions at the vertical cylindrical wall. For the temperature condition, we assume that the temperature at the vertical wall is prescribed and varies parabolically from T_s at the top and bottom to a maximum temperature at the circumference midway between the top and bottom. With the maximum temperature difference along the vertical wall as $(\Delta T)_c$, the temperature condition is

$$T = 1 - z^2 \quad \text{at } r = 1. \tag{1}$$

For the flux condition, we assume that the radial heat flux into the liquid at the vertical wall is prescribed and varies parabolically from zero at the top and bottom to $q_{\max}$ at the circumference midway between the top and bottom. With $(\Delta T)_c = Rq_{\max}/k$, where k is the liquid's thermal conductivity, the flux condition is

$$\frac{\partial T}{\partial r} = 1 - z^2 \quad \text{at } r = 1. \tag{2}$$

Gelfgat et al. [3] presented a solution for the problem treated here with the temperature condition. The primary contribution of the present paper is the extension of their linear stability analysis to the flux condition. The primary justification for the present paper is the revelation that the results for the two thermal boundary conditions at the vertical wall are radically different. The implication for zonal-melting crystal growth is that accurate stability predictions require a very accurate modeling of the heat transfer from the external heater, through the ampoule and into the melt. The results presented here also show that a small change in Pr can radically change the value of the critical Grashof number Gr and the nature of the instability, so that accurate predictions also require a very accurate value for Pr. The values of Pr for most semiconductors are changed by small amounts of additives, and they can change during a crystal-growth process as additives rejected during solidification accumulate in the melt. Therefore the thermal boundary conditions and the thermophysical parameters must precisely reflect the actual process in order to obtain accurate predictions for the instability. Gelfgat et al. [3] treated the range $0.0 \leqslant Pr \leqslant 0.05$, but we have extended the results to the range $0.0 \leqslant Pr \leqslant 0.1$ in order to include a number of important semiconductors, e.g., gallium–arsenide with $Pr = 0.068$ [4].

In the Rayleigh–Benard problem for a vertical cylinder, the top and bottom walls are also isothermal, but the bottom wall is hotter than the top one. The thermal boundary condition at the vertical cylindrical wall is either the adiabatic condition with zero radial heat flux or the conductive condition with a prescribed linear temperature variation from the hot bottom to the cold top. For a small temperature difference between the top and bottom, the liquid is stagnant. At a critical value of the Rayleigh number, $Ra = Pr\,Gr$, there is a transition from a stagnant fluid to a steady axisymmetric or non-axisymmetric flow for smaller or larger height-to-diameter ratios, respectively. For a height-to-diameter ratio of one, Buell and Catton [5] found that the critical values of Ra are 3770 and 8010 for the adiabatic and conductive conditions at the vertical wall, respectively. Both cases involve the transition from a stagnant fluid to a steady, non-axisymmetric convection with an azimuthal wave number $m = 1$. The critical value of Ra for the primary Rayleigh–Benard instability is independent of Pr. Therefore the Rayleigh–Benard instability is also dependent on the thermal boundary condition at the vertical wall.

The present problem is more closely related to the secondary Rayleigh–Benard instability in cylinders with smaller height-to-diameter ratios, i.e., below 0.55 and 0.72 for the adiabatic and conductive conditions, respectively. For these small ratios, the first transition leads to a steady, axisymmetric flow, while the second instability leads from this steady, axisymmetric flow to a periodic non-axisymmetric flow. The secondary instability depends on Pr. Linear stability analyses for the secondary Rayleigh–Benard instability have been presented by Wanschura et al. [6] and by Touihri et al. [7], while a fully nonlinear, three-dimensional numerical simulation was presented by Neumann [8]. For gallium with $Pr = 0.0286$, there is excellent agreement between the predictions of a linear stability analysis and the experimental results for the primary Rayleigh–Benard instability with the adiabatic condition [9].

The present problem is related to the buoyant instability in a vertical cylinder (1) with isothermal top and bottom walls at the same temperature, (2) with a higher-temperature, isothermal band around the central part of the vertical wall and (3) with adiabatic conditions along the vertical wall above and below the isothermal band. Selver et al. [10] presented experimental measurements of the critical Rayleigh number. Rubinov et al. [11] presented a linear stability analysis for this problem. Ma et al. [12] solved the fully nonlinear, three-dimensional equations. The good agreement of the linear stability results [11] with the fully nonlinear, three-dimensional results [12] shows that linear stability analyses give accurate predictions of the critical Rayleigh number and critical frequency for this type of axisymmetric buoyant convection. All three papers [10–12] treat a single value of the Prandtl number, namely $Pr = 0.021$, except for Figs. 15–17 in [11].

2. Problem formulation

With the Boussinesq approximation, the dimensionless equations are

$$\frac{\partial \mathbf{v}}{\partial t} + (\mathbf{v}\cdot\nabla)\mathbf{v} = -\nabla p + GrT\hat{\mathbf{z}} + \nabla^2\mathbf{v}, \tag{3}$$

$$\nabla\cdot\mathbf{v} = 0, \tag{4}$$

$$\frac{\partial T}{\partial t} + \mathbf{v}\cdot\nabla T = \frac{1}{Pr}\nabla^2 T, \tag{5}$$

where (a) t is the time normalized by R^2/ν, (b) $\mathbf{v}$ is the liquid velocity normalized by ν/R, (c) p is the deviation of the dimensional pressure from the hydrostatic pressure for a uniform density ρ, normalized by $\rho\nu^2/R^2$, (d) $\hat{\mathbf{r}}$, $\hat{\theta}$, $\hat{\mathbf{z}}$ are unit vectors for the cylindrical coordinates and (e) ν is the liquid's kinematic viscosity. The dimensionless parameters are

$$Gr = \frac{g\beta(\Delta T)_c R^3}{\nu^2}, \quad Pr = \frac{\nu}{\kappa}, \tag{6}$$

where $g = 9.81\ \mathrm{m/s^2}$, while β and κ are the liquid's volumetric expansion coefficient and thermal diffusivity, respectively. The boundary conditions on the velocity are

$$\mathbf{v} = 0 \quad \text{at } r = 1 \text{ and at } z = \pm 1. \tag{7}$$

For the linear stability analysis, we introduce the form

$$v_r = v_{r0}(r,z) + \varepsilon\mathrm{Real}[v_{r1}(r,z)\exp(\lambda t - im\theta)] \tag{8}$$

for each of the variables v_r, v_θ, v_z, p, T. Here (a) the subscript 0 denotes the variables in the steady, axisymmetric base flow, (b) $v_{\theta 0} = 0$ because there is no azimuthal velocity in the base flow, (c) the subscript 1 denotes the complex modal functions, such as $v_{r1} = v_{r1R} + \mathrm{i}v_{r1I}$, for the small $O(\varepsilon)$ perturbation in the linear stability analysis, (d) $\lambda = \lambda_R + \mathrm{i}\lambda_I$ is the complex eigenvalue and (e) m is the real, integer azimuthal wave number. The base flow and linear perturbation equations neglect $O(\varepsilon)$ and $O(\varepsilon^2)$ terms, respectively.

For the steady, axisymmetric base flow, we introduce the stream function $\psi_0(r,z)$, where

$$v_{r0} = \frac{1}{r}\frac{\partial\psi_0}{\partial z}, \quad v_{z0} = -\frac{1}{r}\frac{\partial\psi_0}{\partial r}, \tag{9}$$

and we eliminate p_0 by cross-differentiating the r and z components of Eq. (3). Therefore the base flow is governed by a fourth-order equation for ψ_0 and a second-order equation for T_0. We represent each of these two base-flow variables by a sum of Chebyshev polynomials in r and z. We insure that the representations have the correct Taylor series in r, i.e., only even powers of r starting with r^2 and 1 for ψ_0 and T_0, respectively. We apply each equation at the Gauss–Lobatto collocation points, including $r = 0$. For each equation at $r = 0$, we identify the leading power of r in the Taylor series of that equation, divide by this power of r and take the limit as $r \to 0$. For each pair of values for Gr and Pr, the nonlinear base-flow equations are solved with an iterative Newton–Raphson scheme.

The complex modal functions v_{r1}, $v_{\theta 1}$, v_{z1}, p_1, T_1 are governed by a set of linear, homogeneous equations and boundary conditions. The governing equations involve coefficients given by the base-flow variables and their first derivatives, and they also involve the complex eigenvalue λ from the time derivatives in Eqs. (3) and (5). We use Eq. (4) to eliminate $v_{\theta 1}$ and we use the azimuthal component of Eq. (3) to eliminate p_1. Therefore we have fourth-order equations governing v_{r1}, v_{z1} and a second-order equation governing T_1. Each perturbation variable is represented by a sum of Chebyshev polynomials in r and z. We insure that each representation has the correct Taylor series in r, so that the representation of v_{r1} includes the powers $r^{(m-1)}, r^{(m+1)}, r^{(m+3)}, r^{(m+5)}, \ldots$ and the representations of v_{z1}, T_1 include the powers $r^m, r^{(m+2)}, r^{(m+4)}, r^{(m+6)}, \ldots$ The perturbation equations are applied at the Gauss–Lobatto collocation points in r and z, including $r = 0$. Again the leading term in the Taylor series of each equation is applied at $r = 0$. The resultant linear matrix eigenvalue problem was solved with two methods. In order to insure that we had all the important eigenvalues, we used the FORTRAN subroutines in the EISPACK library [13]. When we were sure which eigenvalue was the critical one, we used the inverse iteration method [14].

For each pair of values of Pr and Gr, we first used the Newton–Raphson iterative scheme to determine the steady, axisymmetric base flow and then we found the eigenvalues for $m = 1, 2, 3, 4, 5, 6, \ldots$ In general, we would find one point on the neutral stability curve by fixing Pr and increasing Gr until one eigenvalue for one value of m had $\lambda_R = 0$, while all the other eigenvalues for this value of m and for all other values of m had $\lambda_R < 0$. It turns out that the neutral stability curve for the flux condition doubles back on itself, so then we fixed Gr and decreased Pr until we found one point on this curve.

3. Results

We used two comparisons in order to validate the accuracy of our numerical solutions. First, for the temperature condition, we compared our results to those presented by Gelfgat et al. [3]. The agreement is excellent over the entire range $0.0 < Pr < 0.05$. For example, for $Pr = 0.05$ and $m = 2$, they found that the critical value of the Grashof number, $Gr_{cr} = 92{,}343$ with $\lambda_I = 56.401$ [15], and we found that $Gr_{cr} = 92{,}338$ with $\lambda_I = 56.400$. For our second validation, we wrote uniform-grid finite-difference codes for both the base-flow and eigenvalue problems. For the flux condition with $Pr = 0.02$ and $m = 2$, the finite-difference codes gave (a) $Gr_{cr} = 106{,}137$ with $\lambda_I = 57.56$ for a 41×81 grid, (b) $Gr_{cr} = 104{,}510$ with $\lambda_I = 56.75$ for a 61×121 grid, (c) $Gr_{cr} = 103{,}952$ with $\lambda_I = 56.48$ for an 81×161 grid, and (d) $Gr_{cr} = 103{,}696$ with $\lambda_I = 56.35$ for a 101×201 grid, while the spectral codes gave $Gr_{cr} = 103{,}243$ with $\lambda_I = 56.12$ for 22×43 polynomials and for 34×67 polynomials. Similarly for the flux condition with $Pr = 0.1$, the finite-difference codes gave (a) $Gr_{cr} = 115{,}844$ for a 41×81 grid, (b) $Gr_{cr} = 111{,}021$ for a 61×121 grid, (c) $Gr_{cr} = 109{,}403$ for an 81×161 grid, and (d) $Gr_{cr} = 108{,}660$ for a 101×201 grid, while the spectral codes gave $Gr_{cr} = 107{,}449$ for 22×43 polynomials and for 34×67 polynomials. All the results presented here were obtained with the spectral codes with 34 Chebyshev polynomials of r and 67 polynomials of z.

The values of Gr_{cr} for $0.0 \leqslant Pr \leqslant 0.1$ and for both thermal boundary conditions at $r = 1$ are presented in Fig. 1, while $m = 2$ for every critical mode here. For the temperature condition as Pr is increased, Gr_{cr} decreases from 119,577 for $Pr = 0.0$ to a minimum of 92,338 for $Pr = 0.05$ and then increases to 118,663 for $Pr = 0.1$, while the critical mode is periodic throughout this range. For the flux condition, the critical mode is periodic for $0.0 \leqslant Pr \leqslant 0.0288$ and is steady ($\lambda_I = 0$) for $0.0288 \leqslant Pr \leqslant 0.1$. As Pr is increased, Gr_{cr} decreases from 109,624 for $Pr = 0.0$ to a local minimum of 97,050 for $Pr = 0.01$ and then begins to increase. The slope of the neutral stability curve begins to increase dramatically as Pr is increased from 0.025, where $Gr_{cr} = 115{,}637$. Details of the neutral stability curve for the flux condition and for $0.028 \leqslant Pr \leqslant 0.0305$ are presented in Fig. 2. The neutral stability curve has a vertical tangent at $Pr = 0.0284208$ and $Gr = 170{,}000$ and then doubles back to another vertical tangent at $Pr = 0.0280052$ and $Gr = 236{,}000$. The slope decreases from infinity as Pr is increased until there is an abrupt change from a low-frequency periodic mode to a high-frequency periodic mode at $Pr = 0.0285373$ and $Gr_{cr} = 272{,}814$. As Pr is increased from 0.0285373, Gr_{cr} increases only slightly until $Gr_{cr} = 272{,}983$ at $Pr = 0.0288$ when there is an abrupt change from the high-frequency periodic mode to a steady mode. As Pr is increased from 0.0288, Gr_{cr} decreases until it reaches a minimum of 96,654 at $Pr = 0.08$ and then increases to 107,449 at $Pr = 0.1$.

For the temperature condition, the $(\Delta T)_c$ in Gr is the maximum temperature difference along the vertical wall, and for the flux condition, the $(\Delta T)_c$ in Gr is defined from the maximum radial heat flux at the vertical wall. In order to define both Grashof numbers in terms of the maximum temperature difference along the vertical wall, we should compare Gr_{cr} for the temperature condition and $Gr_{cr}T_{max}$ for the flux condition, where T_{max} is the maximum dimensionless temperature which always occurs at $r = 1$. The values of T_{max} for the flux condition are presented in Fig. 3. For very small values of Pr, where there is virtually no convective heat transfer for the critical flow, this correction

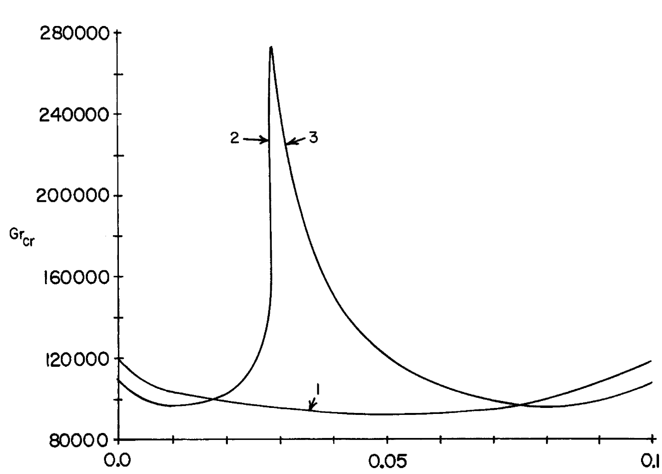

Fig. 1. Critical Grashof number versus Prandtl number for both boundary conditions at $r = 1$ and for $0.0 < Pr < 0.1$. 1 = periodic mode for the temperature condition, 2 = periodic mode for the flux condition, and 3 = steady mode for the flux condition.

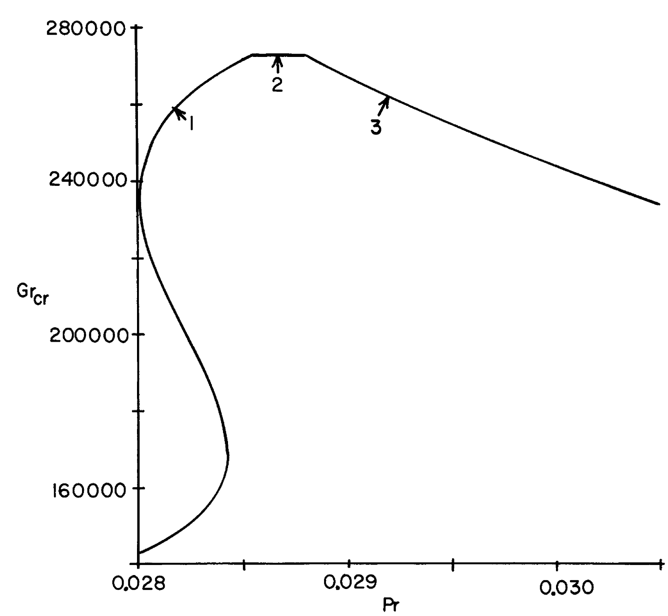

Fig. 2. Critical Grashof number versus Prandtl number for the flux condition and for $0.028 < Pr < 0.0305$. 1 = low-frequency periodic mode, 2 = high-frequency periodic mode, and 3 = steady mode.

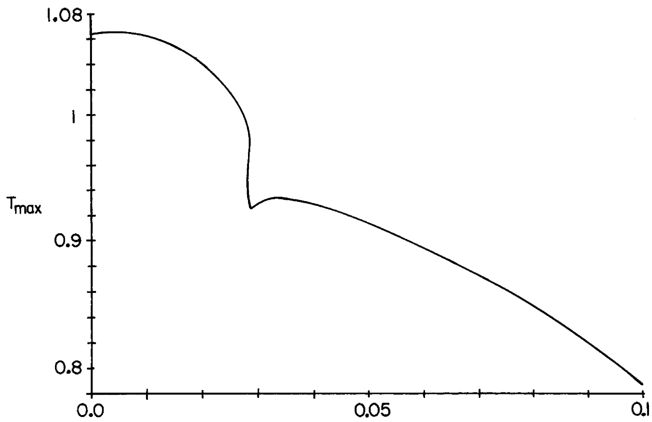

Fig. 3. Maximum dimensionless temperature versus Prandtl number for the flux condition.

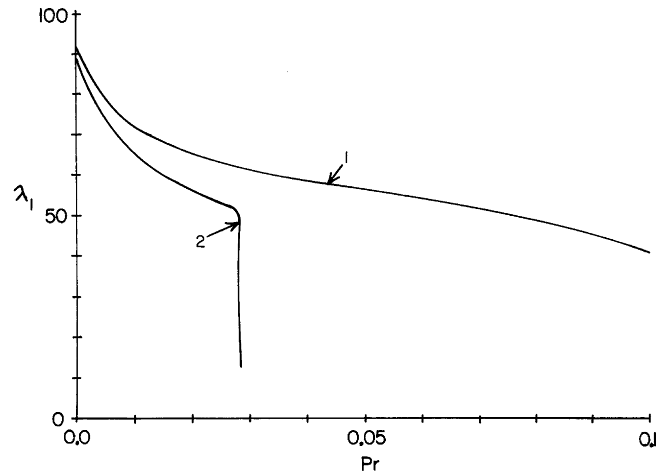

Fig. 4. Dimensionless frequency for the periodic modes. 1 = temperature condition and 2 = low-frequency mode for the flux condition.

leads to closer agreement between the two conditions. For the temperature and flux conditions, respectively, (a) $Gr_{cr} = 119{,}577$ and $Gr_{cr}T_{max} = 116{,}564$ for $Pr = 0.0$, (b) $Gr_{cr} = 107{,}865$ and $Gr_{cr}T_{max} = 105{,}378$ for $Pr = 0.005$, (c) $Gr_{cr} = 103{,}535$ and $Gr_{cr}T_{max} = 103{,}089$ for $Pr = 0.01$, and (d) $Gr_{cr} = 101{,}037$ and $Gr_{cr}T_{max} = 101{,}604$ for $Pr = 0.015$. The two curves in Fig. 1 cross at $Pr = 0.0169$ and $Gr_{cr} = 100{,}306$, so that the T_{max} correction to Gr_{cr} for the flux condition increases the differences between the results for the temperature and flux conditions for $0.0169 < Pr < 0.0275$. For $Pr > 0.0275$, $T_{max} < 1.0$, so that the curve for the flux condition in Fig. 1 is lowered. The correction increases the difference between the curves for larger values of Pr. For $Pr = 0.1$, $Gr_{cr} = 118{,}663$ for the temperature condition and $Gr_{cr}T_{max} = 84{,}411$ for the flux condition. Clearly the difference in the definitions of $(\Delta T)_c$ plays no significant role in the differences between the values of Gr_{cr} for the temperature and flux conditions.

The frequencies λ_I for the temperature condition and for the low-frequency mode for the flux condition are presented in Fig. 4. For the temperature condition, λ_I decreases from 92.06 for $Pr = 0.0$ to 40.75 for $Pr = 0.1$. For the flux condition, λ_I decreases from 89.03 for $Pr = 0.0$ to 50.82 for $Pr = 0.028$. As we move up along the S-shaped curve in Fig. 2 from $Gr_{cr} = 142{,}919$, $Pr = 0.028$ to $Gr_{cr} = 272{,}814$, $Pr = 0.0285373$, λ_I decreases from 50.82 to 12.57. At $Pr = 0.0285373$, there is an abrupt change from the low-frequency mode shown in Fig. 4 to a high-frequency mode. For the high-frequency mode, λ_I decreases from 347.51 for $Pr = 0.0285373$ to 346.09 for $Pr = 0.0288$. For $Pr > 0.0288$, $\lambda_I = 0.0$ for the flux condition.

Some insights into the modal switches for the flux condition are provided by the changes in the values of the first four eigenvalues for $m = 2$ as Pr is decreased from 0.032. For $Pr > 0.0288$, the critical eigenvalue is $\lambda = 0$. The other three eigenvalues of interest for $m = 2$ are: (a) $-14.6 \pm 295i$ and -34.8 for $Pr = 0.032$, (b) $-6.6 \pm 324i$ and -15.5 for $Pr = 0.03$, (c) $-3.6 \pm 334i$ and -8.7 for $Pr = 0.0294$, and (d) $-1.28 \pm 342i$ and -3.99 for $Pr = 0.029$. If the high-frequency complex conjugates are excluded, then (a) as Pr is decreased from 0.032 to 0.02868, the second real eigenvalue increases from -34.8 to 0.0 and Gr_{cr} increases from 211,354 to 276,375, (b) the two real eigenvalues merge at $Pr = 0.02868$ and split into a pair of complex conjugates, and (c) as Pr is decreased from 0.02868 to 0.0280 along the S-shaped curve in Fig. 2, the λ_I for this new pair of complex conjugates increases from 0.0 to 50.82 and Gr_{cr} decreases from 276,375 to 142,919. The peak that occurs at $Pr = 0.02868$, $Gr_{cr} = 276{,}375$, where the two real eigenvalues merge and the frequency of the new complex conjugates begins to increase from zero, is cut off by the high-frequency complex conjugates which are the critical modes for $0.0285373 < Pr < 0.0288$ with $\lambda_I = 346$–347. Further insights are provided by the contour plots of the perturbation variables v_{r1}, v_{z1}, T_1 for the two real eigenvalues just before they merge. Specifically for $Pr = 0.029$, the plots of these variables for the eigenvalue $\lambda = 0$ are virtually identical to those for the eigenvalue $\lambda = -3.99$. Therefore the two merging modes involve the same physical mechanism, rather than two different mechanisms, so that the periodicity of the newly formed complex conjugates does not arise from an oscillation between two different mechanisms.

Neutral stability involves a balance between (a) an energy transfer from the base flow to the perturbation through the terms $(\mathbf{v}_1 \cdot \nabla)\, \mathbf{v}_0$ and $\mathbf{v}_1 \cdot \nabla T_0$ and (b) a loss of perturbation energy through viscous dissipation and thermal conduction. A thermal instability represents one extreme where the key terms are $\mathbf{v}_1 \cdot \nabla T_0$ and the coupling term $GrT_1\hat{\mathbf{z}}$, while the inertial term $(\mathbf{v}_1 \cdot \nabla)\mathbf{v}_0$ plays no role. The primary Rayleigh–Benard instability is purely thermal since $\mathbf{v}_0 = 0$. An inertial instability represents the opposite extreme where the key source term is $(\mathbf{v}_1 \cdot \nabla)\mathbf{v}_0$. For a purely inertial instability, $\mathbf{v}_1 \cdot \nabla T_0$ may produce a non-zero T_1 for $Pr > 0$, but its feedback to the perturbation velocity through $GrT_1\hat{\mathbf{z}}$ is negligible. We used an artificial linear stability problem in order to investigate the relative roles of

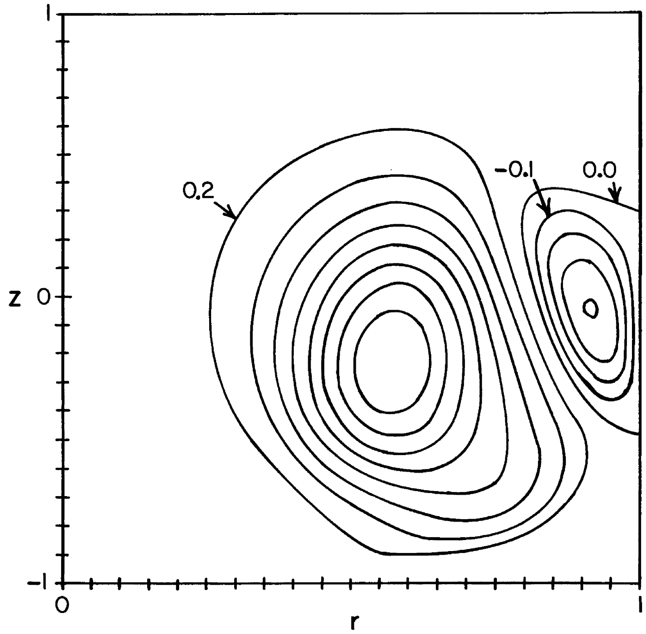

Fig. 5. Contour plot of the perturbation variable v_{z1R} for the steady mode, for $Pr = 0.04$, for $Gr_{cr} = 151{,}199$ and for the flux condition. $v_{z1R} = -0.1k$ for $k = 0$–4 and $v_{z1R} = 0.2k$ for $k = 1$–8.

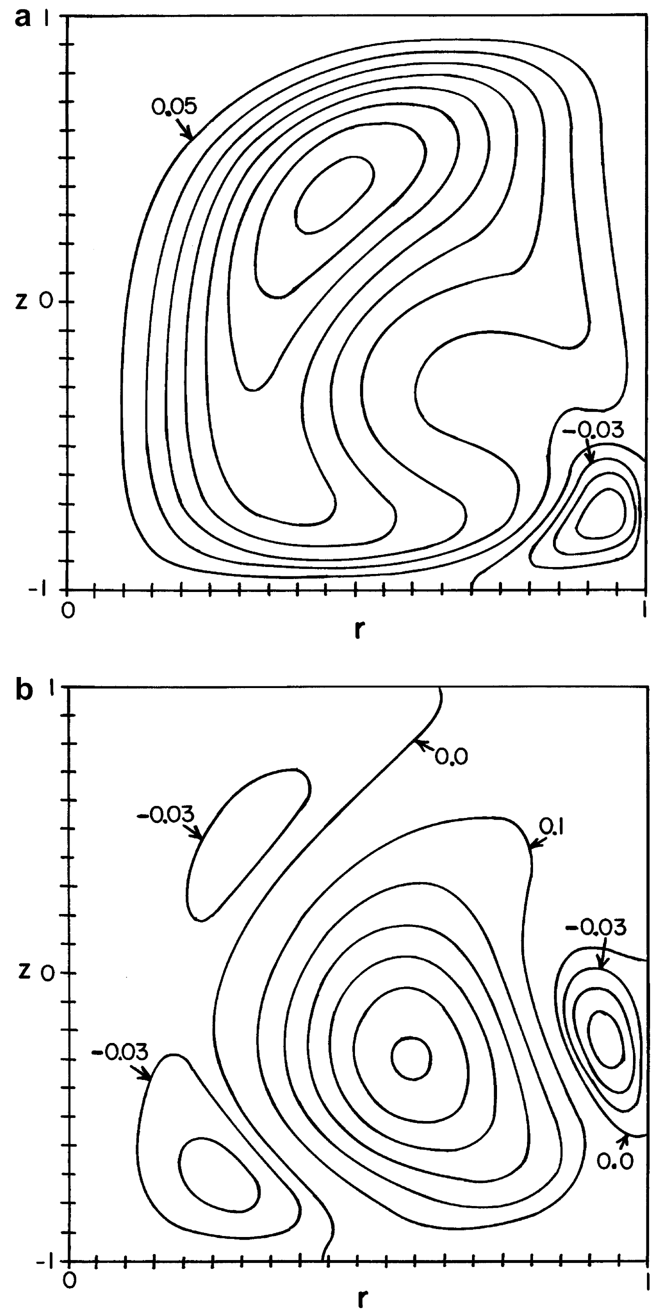

Fig. 6. Contour plots of the perturbation variables v_{z1R} and v_{z1I} for the periodic mode, for $Pr = 0.02$, for $Gr_{cr} = 103{,}243$, for $\lambda_I = 56.12$ and for the flux condition. (a) $v_{z1R} = -0.03k$ for $k = 0$–3 and $v_{z1R} = 0.05k$ for $k = 1$–8. (b) $v_{z1I} = -0.03k$ for $k = 0$–3 and $v_{z1I} = 0.1k$ for $k = 1$–6.

inertial and thermal effects in the present instability for the flux condition. The only difference between the actual and artificial problems is that the term $GrT_1\hat{\mathbf{z}}$ is replaced by zero in the artificial problem. This step eliminates all thermal effects in the instability because the perturbation velocity is now independent of the perturbation temperature and the instability arises entirely from the inertial terms in the momentum equation. Of course, $GrT_0\hat{\mathbf{z}}$ and thermal effects are still important in the base flow. The plots of Gr_{cr} versus Pr for the artificial problem look qualitatively similar to the plots for the flux condition in Figs. 1 and 2, namely, (a) there is a periodic instability below some value of Pr, (b) there is a steady instability above this value of Pr, and (c) there is a large peak of Gr_{cr} at the transition between the steady and periodic instabilities. This similarity indicates that both the periodic and steady instabilities are essentially inertial for $0.0 < Pr < 0.1$. On the other hand, for the artificial problem, the values of Gr_{cr} are significantly different and the transition between the periodic and steady instabilities occurs at a higher value of Pr, relative to the actual problem. Although thermal effects do not play an essential role in the instability, they either augment or oppose the key inertial mechanism enough to shift the locations of the points along the neutral stability curve. Of course the instability is purely inertial for $Pr = 0$ and $Gr_{cr} = 109{,}624$.

For a critical mode, the real form of each perturbation variable is

$$V_{z1}(r,\theta,z,t) = v_{z1R}(r,z)\cos(\lambda_I t - m\theta) - v_{z1I}(r,z)\sin(\lambda_I t - m\theta). \tag{10}$$

For the steady instability for $Pr > 0.0288$, $m = 2$ and $\lambda_I = 0$. The complex perturbation is normalized so that $v_{z1I} = 0$, and Eq. (10) reduces to

$$V_{z1}(r,\theta,z,t) = v_{z1R}(r,z)\cos(2\theta). \tag{11}$$

The contour plot of v_{z1R} for the flux condition with $Pr = 0.04$ is presented in Fig. 5. Because of the θ derivative in the continuity equation, $v_{\theta 1R} = 0$ and $V_{\theta 1} = v_{\theta 1I}(r,z)\sin(2\theta)$, so that there is no perturbation flow across the planes at $\theta = 0, \pm\pi/2$ and π. We need only describe the perturbation flow for

$0 \leqslant \theta \leqslant \pi/2$, because the flow in each of the other three quadrants is given by a reflection across the plane at $\theta = 0$ or at $\theta = \pm\pi/2$. The small region with $v_{z1R} < 0$ near $r = 0.9$ and $z = 0$ in Fig. 5 indicates that a small part of the perturbation flow consists of circulations in $\theta =$ constant planes. At $\theta = 0$, some of the upward flow near $r = 0.7$ and $z = 0$ flows radially outward, axially downward as the negative v_{z1R} in Fig. 5, and then radially inward. This circulation in $\theta =$ constant planes is clockwise for $0 \leqslant \theta < \pi/4$ and counterclockwise for $\pi/4 < \theta \leqslant \pi/2$. Most of the perturbation flow involves a circulation around a radial line in the $\theta = \pi/4$ plane. This circulation consists of axially upward flow for $0 \leqslant \theta < \pi/4$, flow in the $+\theta$ direction across the upper part of the plane at $\theta = \pi/4$, axially downward flow for $\pi/4 < \theta \leqslant \pi/2$, and flow in the $-\theta$ direction across the lower part of the plane at $\theta = \pi/4$.

For the periodic instability for $Pr < 0.0288$, the spatial pattern of the perturbation variables is fixed, and this pattern rotates in the azimuthal direction with a dimensionless angular velocity of λ_I/m. All complex eigenvalues are complex conjugates, and the critical modes with $+\lambda_I$ and $-\lambda_I$ rotate in the $+\theta$ and $-\theta$ directions, respectively. All of the physics of the perturbation flow is revealed by the spatial pattern at $t = 0$, when Eq. (10) reduces to

$$V_{z1}(r,\theta,z,0) = v_{z1R}(r,z)\cos(2\theta) + v_{z1I}(r,z)\sin(2\theta). \qquad (12)$$

The complex perturbation can be multiplied by an arbitrary complex constant. Any normalization fixes the arbitrary location of $\theta = 0$. Our contour plots for v_{z1R} and v_{z1I} for the flux condition with $Pr = 0.02$ and $\lambda_I = 56.12$ are presented in Fig. 6. The contours of v_{z1I} in Fig. 6b are very similar to the contours of v_{z1R} in Fig. 5, and the contours of v_{z1R} in Fig. 6a are qualitatively similar as well, namely, $v_{z1R} > 0$ over most of the plane with a small regions where $v_{z1R} < 0$ near $r = 0.9$. At $t = 0$, $V_{z1} = v_{z1R}$ at $\theta = 0$, $V_{z1} = v_{z1I}$ at $\theta = \pi/4$, $V_{z1} = -v_{z1R}$ at $\theta = \pi/2$, and $V_{z1} = -v_{z1I}$ at $\theta = 3\pi/4$. If the patterns of the contours in Figs. 6a and b were identical, then the perturbation flow would be the same as that for a steady instability, except that the pattern would rotate in the θ direction. Therefore the differences between the patterns of the contours in Figs. 6a and b reveal the differences between the spatial patterns of the perturbation flows for the steady and periodic instabilities. The locations of the regions of negative v_{z1R} and v_{z1I} in Figs. 6a and b indicate that the location of the circulation in $\theta =$ constant planes moves axially back and forth between $z = -0.25$ and $z = -0.75$ as θ varies. For the steady instability, $V_{z1} = 0$ over the entire plane at $\theta = \pi/4 = 0.785$ rad. For a periodic instability, the θ value where $V_{z1} = 0$ is a function of r and z. For example, at $r = 0.45$, $z = 0.4$, $V_{z1} = 0$ at $\theta = 0.857$ rad, and at $r = 0.6$, $z = -0.3$, $V_{z1} = 0$ at $\theta = 1.49$ rad. The maximum values lag the zeros by $\pi/4$ so that the maximum values of V_{z1} occur at $\theta = 0.072$ rad for $r = 0.45$, $z = 0.4$ and at $\theta = 0.705$ rad for $r = 0.6$, $z = -0.3$. Therefore a major difference between the periodic and steady instabilities is that there is an azimuthal phase shift in the perturbation variables for the periodic instability. As a function of time for any $\theta =$ constant plane, V_{z1} would reach its maximum at $r = 0.6$, $z = -0.3$ well before it reached its maximum at $r = 0.45$, $z = 0.4$, and V_{z1} would become negative at $r = 0.6$, $z = -0.3$ while it was still positive at $r = 0.45$, $z = 0.4$. The negative values of v_{z1I} for small values of r in Fig. 6b reflect this azimuthal phase shift because they come from the negative values of $V_{z1} = -v_{z1R}$ at $\theta = \pi/2$ which have an azimuthal lag so that they have not yet become positive at $\theta = \pi/4$.

4. Conclusion

The hydrodynamic instabilities for the heat flux boundary condition given by Eq. (2) are very different from those for the prescribed temperature boundary condition given by Eq. (1). There is a large difference in the values of the critical Grashof number for these two conditions. For the temperature condition, the instability is periodic for the entire range $0.0 < Pr < 0.1$, but for the flux condition, the instability is periodic or steady for $0.0 < Pr < 0.0288$ or $0.0288 < Pr < 0.1$, respectively. For the temperature condition, there is a transition from a periodic instability to a steady one at $Pr = 0.1116$, $Gr_{cr} = 131{,}611$, but this transition does not involve the large local increase in Gr_{cr} that is illustrated in Fig. 2 for the flux condition. Since the characteristics of the instability are very different for these two thermal boundary conditions, accurate instability predictions for zonal-melting crystal growth require very accurate modeling of the heat transfer to the melt and accurate value of the Prandtl number.

Liquid gallium is often used in experiments to investigate crystal-growth processes because its melting temperature is very low. The Prandtl number of 0.0286 for gallium is very close to the large spike of Gr_{cr} in Fig. 2, so stability results for gallium may not be applicable to semiconductors with different values of Pr.

Acknowledgements

This research was supported by the US National Science Foundation under Grant CTS 03-46302 SGER. The authors are grateful to Professor Alexander Gelfgat.

References

[1] N. Imaishi, K. Kakimoto, Convective instability in crystal growth systems, Ann. Rev. Heat Transfer 12 (2002) 187–221.
[2] M. Lappa, Review: Thermal convection and related instabilities in models of crystal growth from the melt on earth and in microgravity. Past history and current status, Cryst. Res. Technol. 40 (2005) 531–549.
[3] A.Yu. Gelfgat, P.Z. Bar-Yoseph, A. Solan, Axisymmetry breaking instabilities of natural convection in a vertical Bridgman growth configuration, J. Cryst. Growth 220 (2000) 316–325.
[4] A.S. Jordan, Estimated thermal diffusivity, Prandtl number and Grashof number of molten GaAs, InP and GaSb, J. Cryst. Growth 71 (1985) 551–558.
[5] J.C. Buell, I. Catton, The effect of wall conduction on the stability of a fluid in a right circular cylinder heated from below, J. Heat Transfer 105 (1983) 255–260.

[6] M. Wanschura, H.C. Kuhlmann, H.J. Rath, Three-dimensional instability of axisymmetric buoyant convection in cylinders heated from below, J. Fluid Mech. 326 (1996) 399–415.
[7] R. Touihri, H. BenHadid, D. Henry, On the onset of convective instabilities in cylindrical cavities heated from below. I. Pure thermal case, Phys. Fluids 11 (1999) 2078–2088.
[8] G. Neumann, Three-dimensional numerical simulation of buoyancy-driven convection in vertical cylinders heated from below, J. Fluid Mech. 214 (1990) 559–578.
[9] J.S. Walker, M.P. Volz, K. Mazuruk, Rayleigh–Benard instability in a vertical cylinder with a rotating magnetic field, Int. J. Heat Mass Transfer 47 (2004) 1877–1887.
[10] R. Selver, Y. Kamotani, S. Ostrach, Natural convection of a liquid metal in vertical circular cylinders heated locally from the side, J. Heat Transfer 120 (1998) 108–114.
[11] A. Rubinov, V. Erenburg, A.Yu. Gelfgat, E. Kit, P.Z. Bar-Yoseph, A. Solan, Three-dimensional instabilities of natural convection flow in a vertical cylinder with partially heated side wall, J. Heat Transfer 126 (2004) 586–599.
[12] D.J. Ma, D. Henry, H. Ben Hadid, Three-dimensional numerical study of natural convection in vertical cylinders partially heated from the side, Phys. Fluids 17 (12) (2005) 124101, 12pp.
[13] B.T. Smith et al., Matrix Eigensystem Routines—EISPACK Guide, second ed.Lecture Notes in Computer Science, vol. 6, Springer, New York, 1976.
[14] Y. Saad, Numerical Methods for Large Eigenvalue Problems, Series in Algorithms and Architectures for Advanced Scientific Computing, Manchester University Press, 1991.
[15] A.Yu. Gelfgat, private communication.